Ultrasonics Sonochemistry 22 (2015) 59–69

Contents lists available at ScienceDirect

Ultrasonics Sonochemistry

journal homepage: www.elsevier.com/locate/ultson

Stable tridimensional bubble clusters in multi-bubble sonoluminescence (MBSL)

J.M. Rosselló *, D. Dellavale, F.J. Bonetto

Instituto Balseiro-CONICET, Centro Atómico Bariloche, Río Negro R8402AGP, Argentina

ARTICLE INFO

Article history:
Received 17 February 2014
Received in revised form 4 June 2014
Accepted 9 June 2014
Available online 17 June 2014

Keywords:
Multi-bubble sonoluminescence (MBSL)
Static pressure
Bi-frequency driving
Positional instability
Bjerknes force
Bubble clusters

ABSTRACT

In the present work, stable clusters made of multiple sonoluminescent bubbles are experimentally and theoretically studied. Argon bubbles were acoustically generated and trapped using bi-frequency driving within a cylindrical chamber filled with a sulfuric acid aqueous solution (SA85w/w). The intensity of the acoustic pressure field was strong enough to sustain, during several minutes, a large number of positionally and spatially fixed (without pseudo-orbits) sonoluminescent bubbles over an ellipsoidally-shaped tridimensional array. The dimensions of the ellipsoids were studied as a function of the amplitude of the applied low-frequency acoustic pressure (P_{Ac}^{LF}) and the static pressure in the fluid (P_0). In order to explain the size and shape of the bubble clusters, we performed a series of numerical simulations of the hydrodynamic forces acting over the bubbles. In both cases the observed experimental behavior was in excellent agreement with the numerical results. The simulations revealed that the positionally stable region, mainly determined by the null primary Bjerknes force ($\vec{F}_{Bj}$), is defined as the outer perimeter of an axisymmetric ellipsoidal cluster centered in the acoustic field antinode. The role of the high-frequency component of the pressure field and the influence of the secondary Bjerknes force are discussed. We also investigate the effect of a change in the concentration of dissolved gas on the positional and spatial instabilities through the cluster dimensions. The experimental and numerical results presented in this paper are potentially useful for further understanding and modeling numerous current research topics regarding multi-bubble phenomena, e.g. forces acting on the bubbles in multi-frequency acoustic fields, transient acoustic cavitation, bubble interactions, structure formation processes, atomic and molecular emissions of equal bubbles and nonlinear or unsteady acoustic pressure fields in bubbly media.

1. Introduction

The spontaneous appearance of gas bubbles in a continuous fluid medium under the action of a high intensity acoustic field is called "acoustic cavitation". The formation of these cavities is promoted by the presence of trapped gas pockets on undissolved microscopic impurities named "cavitation nuclei". Nuclei undergo an explosive bubble expansion when the instantaneous absolute pressure in the liquid falls below their vapor pressure during the negative pressure phase of the acoustic cycle [1,2]. It has been established that the onset of cavitation depends not only on the bulk physical properties of the liquid, but also on the static pressure, frequency and amplitude of the sound, temperature, amount of dissolved gas, and possibly on the wave shape of the sound field [1,3–5].

Cavitation bubbles can be trapped and stabilized in the liquid by means of a stationary acoustic field. Under certain conditions where the acoustic pressure amplitude is above a frontier known as "dynamical Blake threshold", the bubbles undergo strong nonlinear oscillations with the periodicity of the external acoustic field [6]. In that oscillatory regime, the gas bubbles are forced to have a strong spherically converging inertial collapse. This results in a sudden rise in pressure, density and temperature within the bubble, causing the formation of a light emitting hot plasma core [7]. This phenomenon called Sonoluminescence, can be classified into two types depending on the bubbles mean "lifetime". In "transient" cavitation the bubbles do not last longer than a few acoustic cycles [8], whereas in "stable" sonoluminescence bubbles do not dissolve nor breaks, and can be held as long as the bubble environment remains unchanged [9–12]. In the stable case, a bubble can be positionally unstable changing its mean position inside the acoustic resonator, or spatially unstable describing quasiperiodic orbits around a constant mean position.

* Corresponding author.
E-mail address: jrossello@cab.cnea.gov.ar (J.M. Rosselló).

http://dx.doi.org/10.1016/j.ultsonch.2014.06.003
1350-4177/

In 2005 Flannigan and Suslick [13], and Troia et al. [14], showed that the use of highly viscous and low vapor pressure fluids, such as sulfuric or phosphoric acid aqueous solutions (SA and PA, respectively), led to an important increase in the light emitted by the bubbles (compared to similar experiments using water). Urteaga and Bonetto [15] were able to significantly reduce the orbits of a luminescent bubble in SA adding a harmonic of the fundamental frequency to the ultrasound signal. In 2012, Dellavale et al. [16,17] performed single bubble sonoluminescence (SBSL) experiments using strongly degassed SA (with Xe or Ar) and showed that the orbits can also be suppressed when low relative concentration of dissolved gas are used. Recently, Rechiman et al. [18] reproduced those experimental results by means of a numerical code that solves the bubble radial dynamics coupled with the translational dynamics and discussed the role of the various forces acting over the bubble on the positional and spatial instabilities. In SBSL with SA the limiting agent over the acoustic pressure that could be applied on the bubble is mainly given by the primary Bjerknes force, whose effect is to displace the bubble away from the pressure antinode [12,16–18]. In 2013, we showed through experiments and numerical simulations in SA that an increase in the static pressure (P_0) shifts the positional instability frontier to higher acoustic pressures, which resulted in a significant increase of the energy focusing during the bubble collapse [19].

The idea of having a system of multiple bubbles collapsing synchronously to generate a converging high pressure shockwave, or study their collective behavior to enhance the efficiency of energy conversion in multi-bubble sonoluminescence (MBSL) has been of interest of many researchers [20,21]. In addition, the application of bubble clustering in topics like sonochemistry, ultrasonic degassing, therapeutic cavitation, high contrast flow imaging and erosion damage, motivated many experimental and numerical studies to shed light upon several unresolved topics related to multi-bubble cavitation. Usually, the cavitation bubbles clusters develop filamentary patterns or bubble webs [22,23], luminescent streamers [23,24] or non uniform bubble clouds [21,25]. All these conformations have a transient behavior. Bubble clusters with periodical patterns could be observed in sonochemical experiments [5,26,27]. The latter demonstrated the correlation between the distribution of moving bubbles and the external acoustic field. There are few experimental works in the current literature which report bubble structures composed of spatially stable (fixed) bubbles. Posakony et al. [28] achieved the generation of a stable tridimensional multi-bubble pattern but their analysis was limited to a simulation of the imposed acoustic field. Troia et al. [14] report a "bubble lattice" composed of nearly fixed bubbles but the fact that the structure matched the vessel boundaries suggest that this phenomenon is simply explained by the action of primary Bjerknes force pushing the bubbles over the chamber walls. The numerical works about multi-bubble systems done in the last decade agreed that the bubble interactions have a suppressor effect on the bubble expansion. This fact explains why the observed light pulses in MBSL are always dimmer than those in SBSL [29]. The main reasons reported for this reduction in the bubbles collapse violence are: The positive pressure wave emitted by the bubbles in the expansion phase suppresses the expansion of neighbor bubbles [30]; the bubbles interaction deforms their shape making the collapses nonspherical and preventing them to attain high energy concentrations [20]; and the acoustic amplitude is strongly reduced by the presence of the bubbles (bubble screening) [20,25]. Another important mechanism by which bubbles interact is the secondary Bjerknes force. The secondary Bjerknes force could be attractive or repulsive depending mainly on the relative size of the bubbles [6], the distance between them [29], the fluid properties [31], the driving frequency, and amplitude of the acoustic field [6,32]. Rabaud et al. [33] succeeded to generate a bidimensional "acoustically bound bubble crystal" proving that there is a finite equilibrium distance between oscillating bubbles.

In this work, stable clusters made of multiple sonoluminescent argon bubbles in a sulfuric acid aqueous solution (SA85w/w) were experimentally and theoretically studied. All the cavitation bubbles were positionally and spatially stable, achieving a degree of control on the luminescent bubble cluster with no precedent in the current scientific literature. In order to give a theoretical background to the size and shape of the bubble clusters for different acoustic pressures and various static pressures, a series of numerical simulations of the hydrodynamic forces acting on the bubbles are discussed.

2. Experimental method

The experiments were made using the cylindrical acoustic chamber described in Ref. [19]. Details of the electronics and equipments employed can be found as well in Ref. [19] and references therein. The working fluid was a sulfuric acid aqueous solution 85% w/w (SA85) with argon gas dissolved. The resonance frequency of the apparatus for the lowest order axisymmetric oscillation mode with a pressure antinode in the geometrical center of the flask, was experimentally determined in approximately $f_0 = 30.35$ kHz. The driving system was composed of four equal piezoceramics transducers (PZT) attached to the outer cylinder wall in opposite pairs. Two opposite drivers (PZT_{LF}) were used for a low-frequency signal (f_0; V_{PZT}^{LF}), while the remaining pair (PZT_{HF}) was used for a high-frequency signal, which was set to be a harmonic of f_0 (Nf_0). A disc shaped pill PZT was used as a microphone (MIC). The quality factor (Q) of the system was measured (in absence of bubbles) for the main resonance, the tenth and the eleventh harmonic being approximately 220, 1200 and 2200 respectively.

Standard Mie scattering technique [34] was used to determine the temporal evolution of the bubble radius. The room temperature was controlled to be 300 K during the experiments. The experimental data traces were processed and fitted employing the numerical model of the bubble dynamics described in Refs. [35–37]. This model was also used to carry out all the numerical simulations presented in this work. The values of the physical properties of the liquid used in the simulations are summarized in Ref. [19].

The position, stability and relative intensity of the studied SL bubbles, were evaluated through photographs captured using a *Nikkon D40x* camera. The number and distribution of bubbles in the pictures were analyzed using a state-of-the-art numerical code.

3. Results and discussion

In this study, the experimental data is constituted by a large number of photographs used to determine the principal characteristics of the bubble clusters (dimensions, number of bubbles, stability of the bubbles, brightness, etc.) and voltage traces of the radius temporal evolution of one of the bubbles to determine, by means of a numerical fit, the following dynamical parameters: bubble ambient radius R_0, low-frequency acoustic pressure on the bubble $P_{Ac}^{LF}|_b$, high-frequency acoustic pressure on the bubble $P_{Ac}^{HF}|_b$, relative gas concentration c_∞/c_0 and relative phase between the driving frequencies ϕ. In what follows we will refer to the low (or high) frequency acoustic pressure amplitude at the antinode as $P_{Ac}^{LF}|_0$ (or $P_{Ac}^{HF}|_0$), and we will refer to P_{Ac}^{LF} (or P_{Ac}^{HF}) when we mention the low (or high) frequency acoustic pressure field in a general sense. The relative phase was defined positive when the high frequency was advanced with respect to the low frequency. The work was divided into two principal experiments. In the first one, we

investigate the dimensions of the hollow cluster of bubbles as a function of the $P_{Ac}^{LF}|_0$ through the low-frequency signal amplitude (V_{PZT}^{LF}). In the second experiment we investigated the effect of the static pressure over a bubble cluster as an extension to the observations reported in Ref. [19] for a single bubble case. This section is divided in several subsections. In Section 3.1 the bubble cluster generation process is described in detail, in Section 3.1.1 we present experimental results and methods related to the influence of the acoustic pressure on the bubble clusters, in Section 3.1.2 photographic material of the effect of P_0 on the clusters is analyzed, and in Section 3.1.3 statistics on the number of bubbles on the perimeter of the clusters and the distance between bubbles are discussed. Section 3.2 details all the assumptions made for the numerical calculations of the acoustic field and the forces involved. Then, the experiments and simulations are compared and discussed in Sections 3.2.1 and 3.2.2. Finally, in Section 3.2.3 we evaluate by means of numerical simulations the influence of c_∞/c_0 on the computed clusters size.

3.1. Sonoluminescent bubble clusters

Multiple cavitation bubbles were generated in the bulk of the fluid by means of a bi-frequency acoustic pressure field composed of a fundamental frequency of $f_0 \sim 30.7$ kHz besides a high-frequency harmonic ($N = 10$ or $N = 11$). Setting the nearest harmonics matching the measured PZT resonance frequency ($N = 11$), we were able to tune the entire system to attain the maximum harmonic amplitude (which has a response peak in the spectrum of the vessel). The generation process of cavitation bubbles under this regime is shown in Fig. 1(a). The latter was captured by illuminating the vessel with a laser plane (2 mm in width) collinear to the symmetry axis of the cylinder. The bubbles appeared near the center of the flask (where a pressure antinode is located for the lowest order axisymmetric oscillation mode at $f_0 \sim 30.35$ kHz) and shift away rapidly from the high pressure region leaving a stream. The streamers stopped when a translational equilibrium position was reached and the bubbles started to emit SL pulses. While the applied ultrasonic excitation was maintained, the system kept generating cavitation bubbles which travelled to different equilibrium positions for few minutes until the cavitation events ceased. There is a combination of physical processes involved in the achievement of this equilibrium state. A large number of bubbles coexisting simultaneously in the fluid detune the resonator [8] by changing the effective acoustic radiation resistance of the liquid [25]. Dezhkunov et al. [20] also states that the energy of the field is distributed (absorbed) and scattered by the bubbles. In both, there is a resultant decrease in the intensity of the ultrasonic field. This can lower the levels of the negative pressure amplitude below the needed level to expand the cavitation nuclei. Another suppressing mechanism is given by Ida et al. in Ref. [30]. In that work numerical simulations of the interaction of bubbles distributed in the edges of regular polygons reveal that the positive pressure waves emitted by the bubbles in their expansion phase could locally increase the absolute pressure, suppressing cavitation events at nearby nucleation centers.

Few minutes after the cavitation onset, the system reached a steady state where spatially fixed (without orbits) SL bubbles are arranged over an ellipsoidal-like tridimensional surface as shown in Fig. 1(b). In Fig. 1(c) we also present a case where the level of dissolved gas was high enough to spatially destabilize the bubbles (onset of pseudo-orbital movement). It is worth mentioning that different instabilities (positional, spatial, diffusive and shape) act as a filter over the kind of bubbles that remain in the cluster. On one hand, the action of primary Bjerknes force separates the bubbles by their size, driving the bubbles with R_0 smaller than the resonance radius (Minnaert radius) to an antinode, bigger bubbles to a pressure node and middle size bubbles reach positional stability at an intermediate P_{Ac}^{LF} [11,23]. Middle size bubbles were experimentally characterized and theoretically

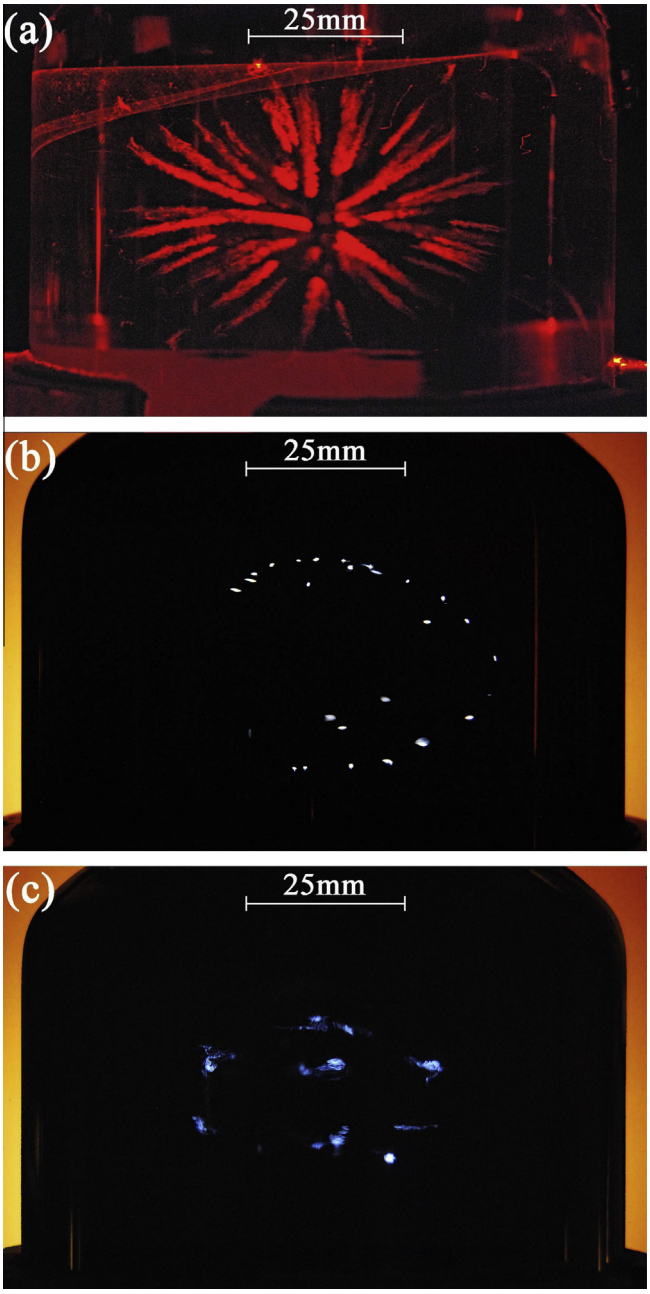

Fig. 1. Ellipsoidal bubble clusters in a cylindrical Pyrex resonator filled with SA85. The pictures were taken setting the camera exposure time to 2.5 s. The static pressure in the fluid was 925 mbar. (a) Ellipsoid generation process captured by illuminating the vessel with a laser plane (2 mm in width) collinear to the symmetry axis of the flask. In this case the bubbles were composed of air and the SA was highly degassed. In the experiment the cavitation bubbles generated near the center of the main pressure antinode shift rapidly from the high pressure region leaving a stream. The bubbles stop when they reach a translational equilibrium position on an oblate ellipsoidal surface. The applied voltage on the piezoelectric transducers was $83V_{rms}$ and the fundamental frequency of $f_0 = 30.35$ kHz. (b) Ellipsoidal bubble cluster in an Argon-SA85 system with a relative gas concentration of $\sim 46 \times 10^{-3}$. The excitation frequencies were $f_0 = 30.78$ kHz and $11f_0$, meanwhile the voltages were $V_{PZT}^{LF} = 62V_{rms}$ and $V_{PZT}^{HF} = 84V_{rms}$. The Q factor for this resonant mode was measured in approximately 2200. (c) Ellipsoidal bubble cluster in an Argon-SA85 system with a relative concentration above 90×10^{-3} and the same driving frequencies of the case showed in (b). Under these conditions, the bubbles were no longer spatially stable (they describe pseudo-orbital movement) and the observed relative number of bubbles was lesser than the case in (b).

explained in [12] and then named as "intermediate bubbles" in the theoretical work [38]. Bubbles with a big ambient radius (e.g. the ones which are the product of coalescence of two bubbles) could break up into several smaller bubbles under the action of Rayleigh–Taylor, parametric or afterbounce instabilities [39]. Then, after the rupture, the smaller bubbles will eventually dissolve (bubble extinction) and the others will achieve an equilibrium ambient radius by rectified diffusion. If we assume an ideal framework where bubble interactions can be neglected and the stationary acoustic field is not significantly distorted by the bubbles, only one kind of bubbles will remain trapped in the field after some time.

We observed that many of the bubbles forming the clusters were arranged in filaments as reported in Refs. [22,23] for non luminescent bubble web structures. However, the bubbles near the poles of the oblate ellipsoid (where the density of bubbles was greater) were distributed over a surface. A detailed visualization of the discussed phenomena was obtained superimposing several photographs of the bubble clusters taken with the same experimental conditions. The camera settings were configured to take saturated images in order to increase the sensitivity of the device and capture the most number of SL bubbles trapped in the flask.

We observed that when the low-frequency excitation signal was suddenly turned off the bubbles dispersed over the entire volume of the resonator and the emission of SL pulses ceased, although the bubbles remain trapped in the fluid as long as the high-frequency wave was applied. In this situation, if V_{PZT}^{LF} was turned on again most of the dispersed bubbles shift to form the previous oblate ellipsoidal cluster. The spatial distribution of bubbles over the perimeter of the ellipsoid may suffer a rearrangement because of the low pressure transitory occurring with every bubble incorporated to the cluster. In contrast, if the high-frequency signal was removed, trapping the bubbles became more difficult for high values of $P_{Ac}^{LF}|_0$. In this case the bubbles become spatially unstable and many of them coalesced generating bubbles with a variety of R_0, therefore a stable structure was no longer observed. We performed trials with different harmonics and found that this parameter was clearly correlated with the number of bubbles trapped in the fluid. Higher harmonic promoted a major number of cavitation bubbles forming the structure. Qualitatively, this fact may be explained considering that the complexity of the acoustic field and the number of local antinodes is greater for higher harmonics. Another interesting fact noticed during the experiments is the dependence of the bubbles positional and spatial stability on the relative phase between the LF and HF driving signals (α) for the cases with low harmonics applied ($N < 6$). We were able to change the bubbles mean position and size of the pseudo-orbits described by the bubbles by modifying α (this phase could differ from the effectively applied to the bubble ϕ).

3.1.1. Acoustic pressure dependence of bubble clusters

In this section we present experimental results on the dependence of the bubble clusters with $P_{Ac}^{LF}|_0$ through the variation of the low-frequency signal amplitude applied to the PZT_{LF} pair (V_{PZT}^{LF}). The measuring procedure used during this experiment can be described as follows. First of all, we measured the radius temporal evolution of a single SL bubble slightly away from the pressure antinode in the center of the flask (i.e. $P_{Ac}^{LF}|_b$ has a limiting value determined by the onset of the positional instability, thus a further increase in $P_{Ac}^{LF}|_0$ did not change the bubble radius dynamics [12]). Then we obtained the dynamical parameters on the bubble $P_{Ac}^{LF}|_b$, $P_{Ac}^{HF}|_b$ and the relative concentration of dissolved gas in the fluid c_∞/c_0, by means of a numerical fit. Next, in absence of bubbles in the fluid we first applied V_{PZT}^{HF} with the eleventh or the tenth harmonic of f_0 set, then V_{PZT}^{LF} was turned on at its maximum value ($\sim 83V_{rms}$) in order to generate as many cavitation bubbles as possible (the cavitation voltage threshold, in absence of bubbles in the liquid, for the experimental conditions detailed in the caption of Fig. 1(b) was $\sim 50V_{rms}$). Right after the rate of cavitation events was significantly reduced, we drove V_{PZT}^{LF} to a specific value between $20V_{rms}$ and $80V_{rms}$. As the acoustic pressure was decreased, many bubbles coalesced or dissolved and only a fraction of the original number of bubbles remain trapped in the fluid and, once an equilibrium state was achieved, the ellipsoidal clusters were formed. An example of the resultant cluster for different values of V_{PZT}^{LF} is shown in Fig. 2. For each driving voltage we took several photographs repeating the aforementioned procedure in its entirety. The photographs show that the number of bubbles and dimensions of the cluster were increased continuously with a raise in V_{PZT}^{LF}. Besides, we observed that the amplitude of the harmonic signal does not appear to significantly modify the structure geometry, although it played an important role in the spatial stabilization of the sonoluminescent bubbles [18]. This behavior suggests that the bubbles on the cluster are near the positional stability frontier of the $R_0 - P_{Ac}^{LF}|_b$ parameter space (if strong bubble interaction is neglected) similarly to the observed in SBSL [12,16,17]. It is important to remark that this kind of bubble structures is "self-assembling" in the sense that specific dynamical and thermodynamic equilibrium situations cannot be totally controlled. For example, if $P_{Ac}^{LF}|_0$ is decreased in order to attain a more compact structure many bubbles will coalesce and the number of bubbles will reduce maintaining the distance (d) between them. Conversely, if $P_{Ac}^{LF}|_0$ is increased the ellipsoid expands but as new

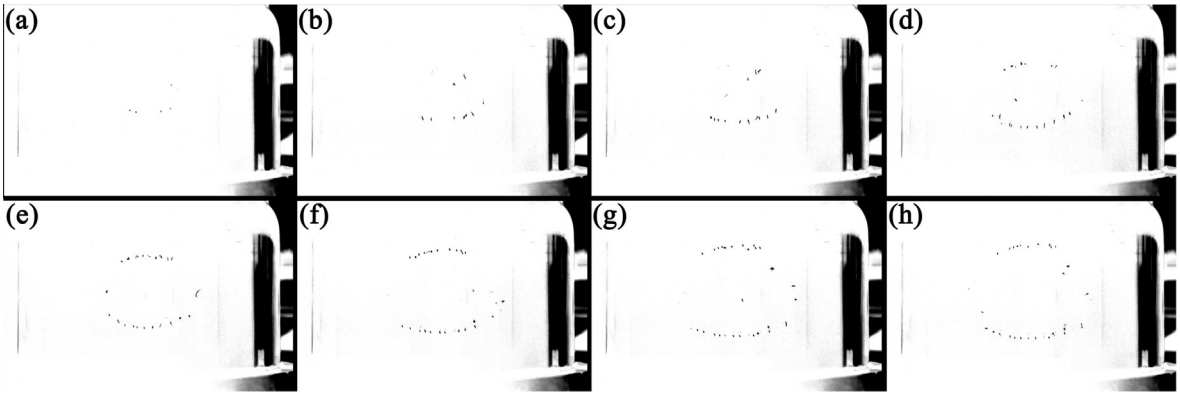

Fig. 2. Ellipsoidal bubble clusters for various low-frequency driving voltages (V_{PZT}^{LF}) in an Argon-SA85 system. The images are the monochrome negative of the original pictures. The static pressure in the fluid was 925 mbar (atmospheric pressure in Bariloche, Argentina) and $c_\infty/c_0 \sim 5 \times 10^{-3}$. The system was driven at a fundamental frequency of $f_0 = 30.73$ kHz besides the eleventh harmonic ($N = 11$). The camera settings were: Iso level = 3200, a lens aperture of f/10 and a shutter speed of 1.6 s. V_{PZT}^{LF} has been varied between $23V_{rms}$ and $80V_{rms}$. (a) $23V_{rms}$; (b) $30V_{rms}$; (c) $35V_{rms}$; (d) $40V_{rms}$; (e) $50V_{rms}$; (f) $60V_{rms}$; (g) $70V_{rms}$ and (h) $80V_{rms}$.

cavitation bubbles appears, d will be almost the same (see Fig. 4). Some degree of control over those parameters could be achieved changing the HF component which determines the complex nodal pattern of the acoustic field.

3.1.2. Effect of P_0 over the multi-bubble system

For the sake of studying the effect of the static pressure on the bubble cluster we repeated the procedure detailed in Section (3.1.1), but in this case the applied voltage on the PZT_{LF} transducers V_{PZT}^{LF} was set to a constant value of $60V_{rms}$ for a given P_0 in a range between 0.4 bar and 1.7 bar. Subsequently, the system started producing bubbles for a couple of minutes until cavitation events ceased due to some of the mechanisms discussed in Section 3.1. Fig. 3 presents a photograph superposition made for four different static pressures in the acoustic chamber (0.75 bar, 0.925 bar, 1.3 bar and 1.5 bar). The change on the dimensions of the resultant oblate ellipsoidal clusters for different P_0 is evident. For low P_0 the ambient radius of the bubbles (R_0) is large, the collapses are less violent [19] and therefore the light produced is dim. In this situation we found that the number of bubbles is relatively large and some of the bubbles were not emitting intense light pulses but can still be observed with the naked eye or by means of an expanded He–Ne laser beam. Those observations are consistent with the numerical predictions on the suppressive effect in the bubble expansion rates due to interactions [30]. As long as the static pressure was increased, the ellipsoidal cluster shrank and the number of bubbles composing the cluster was reduced, meanwhile the light flashes were certainly intensified. It should be noticed that in the photographs of Fig. 3 the camera lens aperture and the exposure time had to be reduced to acquire a similar saturation level with increased P_0. These observations are consistent with the change in the Bjerknes stability frontier as a function of P_0 and the analysis of the dynamical parameters discussed in Ref. [19].

3.1.3. Statistics on the bubble distribution

Statistics on the number of bubbles and the distance among bubbles were performed using a state-of-the-art code in order to compute the mean number of sonoluminescent bubbles (MBN) and the mean nearest neighbor distance on the plane of the photograph (MNN). The values of MBN and MNN are summarized in Fig. 4 for different experimental conditions. The MNN distance is defined as the projected length of the separation vector between two nearest bubbles on the focal plane of the camera lens. The latter was located approximately over the rz plane containing the cylinder axis. Fig. 4(a) and (c) show that there was a nonlinear increase in the mean number of bubbles as $P_{Ac}^{LF}|_0$ was increased, while there was a decrease when P_0 was augmented. Another interesting fact depicted in Fig. 4 (b) is that the MNN for the cases where V_{PZT}^{LF} was increased found a plateau beyond $\sim 50V_{rms}$. We also analyzed (not shown) the distance to second nearest neighbors of the bubbles finding a similar behavior. This suggests that there was some degree of homogeneity or a pattern in the distribution of the bubbles over the ellipsoidal cluster. Previous works about MBSL have shown that these patterns are directly related to the antinode distribution in the acoustic field [5,26–28]. Unfortunately, as discussed in the following sections, we could not establish an clear relation between the bubble structure and the HF antinode distribution.

The measured data of the bubble radius temporal evolution revealed the lack of synchronism of the bubbles constituting the ellipsoids. We found a typical temporal spread in the SL pulses

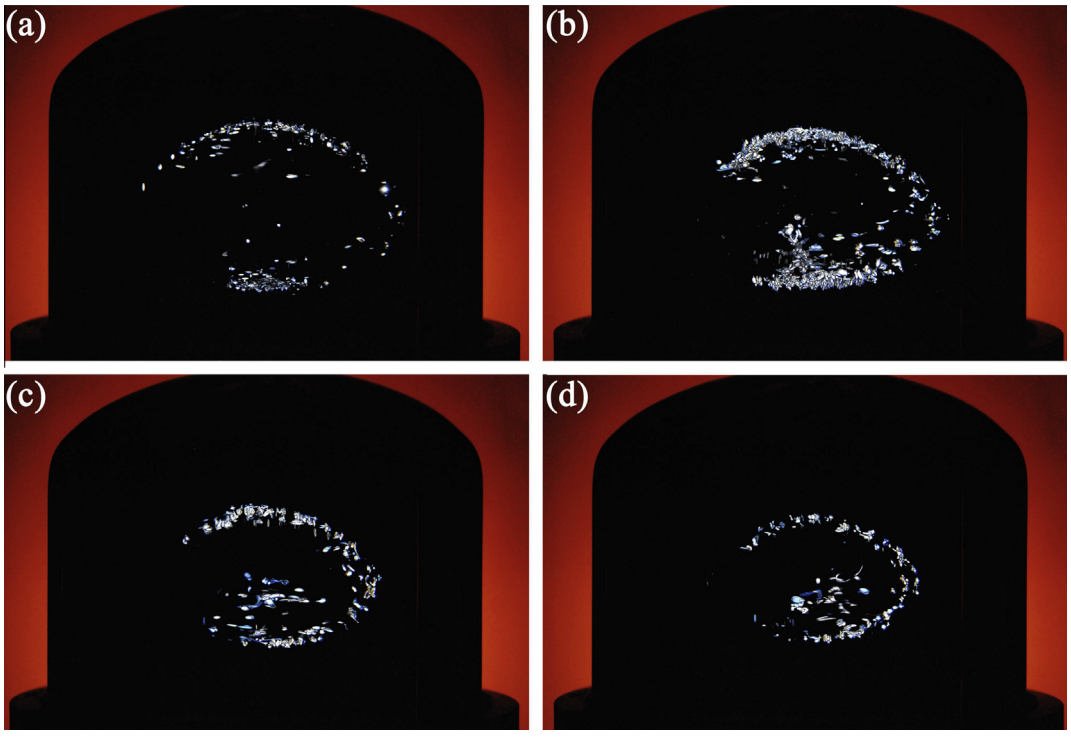

Fig. 3. (Ellipsoidal bubble clusters for different static pressures (P_0) in an Argon-SA85 system. Each image is the result of a superposition of several photographs of bubble clusters with identical conditions. The photographs were taken with a fixed driving voltage of $V_{PZT}^{LF}|_0 = (60.0 \pm 0.4)V_{rms}$. The system was driven with a biharmonic signal of $f_0 = 30.78$ kHz and the eleventh harmonic ($N = 11$). The parameters associated with these measurements are summarized as follows: (a) $P_0 = (750 \pm 15)$ mbar; number of superimposed photographs (N_{ph}): 72; camera settings: Iso level = 3200, a lens aperture of f/5.3 and a shutter speed of 5 s. (b) $P_0 = (925 \pm 15)$ mbar; N_{ph} : 116; camera: Iso level = 3200, f/9 and 1.6 s. (c) $P_0 = (1300 \pm 15)$ mbar; N_{ph} : 76; camera: Iso level = 3200, f/10 and 1 s. (d) $P_0 = (1500 \pm 15)$ mbar; N_{ph} : 90; camera: Iso level = 3200, f/10 and 0.625 s of exposure.

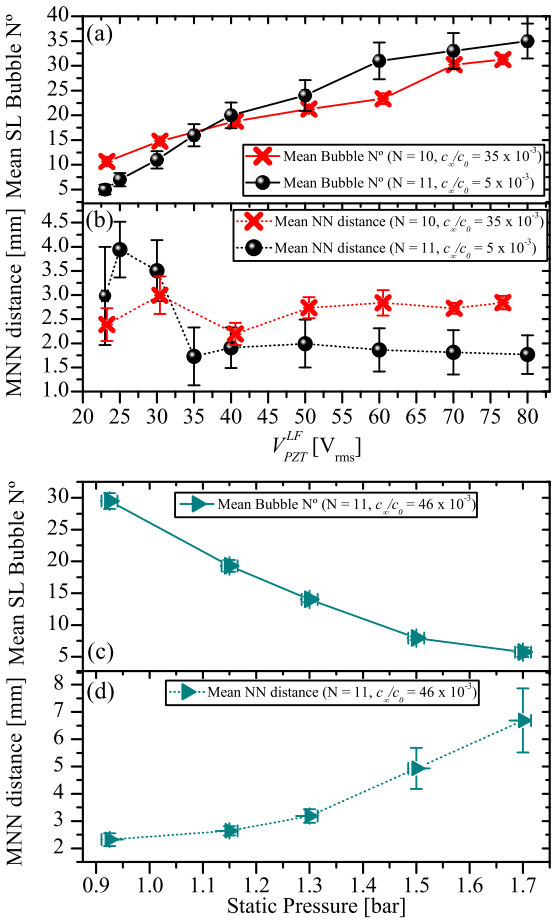

Fig. 4. Mean SL bubble number in the clusters and mean nearest neighbor (MNN) distance as a function of the applied PZT voltage or the static pressure. The MNN distance is defined as the projected length of the separation vector between two nearest bubbles on the focal plane of the camera lens. The latter was located approximately over the *rz* plane containing the cylinder axis. (a) The number of SL bubbles in the graph is given by the number of the remaining bubbles trapped by the ultrasound field once the driving voltage was lowered below the cavitation threshold ($V_{PZT}^{LF} \sim 50 V_{rms}$) from a initial state with $V_{PZT}^{LF} \sim 83 V_{rms}$. (b) The MNN distance converges to a value around 2.78 mm for the case harmonic $N = 10$ and 1.8 mm for $N = 11$. This suggests that there was some grade of homogeneity or a pattern in the distribution of the bubbles over the ellipsoidal surface. (c) In this case the count was done on the bubbles that could be trapped before the detuning of the acoustic chamber drops the pressure amplitude in the antinode to a specific equilibrium value given by $P_{Ac}^{LF}|_0^* = P_{cav} + P_0$. For static pressures below 925 mbar there were some bubbles whose luminescence was dimmer and were not captured in the photographs, thus the digital bubble counting method was no longer accurate for those cases. (d) The MNN distance for this case is well correlated with the number of bubbles forming the cluster. As the bubble number drops, the distance between the remaining bubbles grows rapidly, contrarily to the results found in (b).

between 0.05 μs and 1 μs. These delays cannot be caused by the difference in the optical path of the light pulses since they are the order of picoseconds. It is worth noting that a similar spread in the time of collapse (t_c) was found in SBSL experiments in SA, for a moving bubble and single frequency driving, and a fixed bubble with bi-frequency driving as reported in Refs. [12,16,17]. In the case of moving bubbles the spread in t_c was explained by the change in $P_{Ac}^{LF}|_b$ as the bubbles drift to different positions of the stationary acoustic field. For the case of a fixed bubble, the fluctuations in t_c are believed to be caused by a perturbation on the bubble induced by the reflections of the outgoing shockwave (generated during the bubble collapse) on the resonator walls [8]. On the other hand, for the case of MBSL, Mettin et al. [6] state that in a fluid with sound velocity c there is a time delay $\tau = d/c$ between an oscillation of a bubble and the action of its pressure P_i on a second bubble at a distance d. For $d = 1.8$ mm, which is the mean distance between bubbles obtained with $N = 11$, the delay time is $\tau = 1.2$ μs. As mentioned before in the text, a similar conclusion of the bubble interaction mechanism is proposed by Ida et al. [30]. In spite of the particular reasons for this temporal spread of SL pulses, its effect on the computed positional stability was found to be negligible, thus it will be investigated elsewhere since it is not in the scope of this paper.

The reduction in MBN as P_0 was increased is related to the linear shift to upper values in the cavitation pressure threshold (P_{cav}) reported by Strasberg, Greenspan et al. and Herbert et al. in Refs. [2–4]. As P_0 was increased, the MNN increased nonlinearly resulting from the interplay between the reduction in the MBN and the shrinkage of the ellipsoidal cluster. For static pressures below 925 mbar there were some bubbles whose luminescence was dimmer and were not captured properly in the photographs, thus the digital bubble counting method was no longer accurate for those cases.

3.2. Comparison of the experimental bubble clusters with numerical simulations

In order to give a theoretical interpretation to the size and shape of the bubble clusters described in previous sections, a series of numerical simulations of the hydrodynamic forces acting over the bubbles were performed. The positional and spatial stability of the bubbles is given by the balance among the following forces: Primary Bjerknes force ($\vec{F}_{Bj}$), Buoyancy force ($\vec{F}_{grav}$), Drag force ($\vec{F}_{drag}$), Added mass force ($\vec{F}_{am}$), History force ($\vec{F}_{hist}$) [9–11,17,23] and if we consider bubble interactions, Secondary Bjerknes force ($\vec{F}_{Bj}^{(2)}$) [6,31–33]. In cases where positional and spatial stability are achieved by means of the use of low c_∞/c_0 and high-frequency harmonic driving, $\vec{F}_{drag}$, $\vec{F}_{am}$ and $\vec{F}_{hist}$ have little effect in the positional stability when compared with $\vec{F}_{Bj}$ [12,17], therefore these forces were not included in the numerical calculations described in the subsequent sections. The primary Bjerknes force $\vec{F}_{Bj} = -4\pi/3\tau \int_\tau (R(t))^3 \vec{\nabla} P_{Ac}(\vec{r},t) dt$ depends not only in the bubble radial dynamics ($R(t)$), but also on the gradient of the acoustic pressure field ($\vec{\nabla} P_{Ac}(\vec{r},t)$) and f_0 through the period $= 1/f_0$. Then, using the analytical solution of the wave equation in cylindrical coordinates with perfectly stiff walls boundary conditions [26], we simulated the acoustic field for the lowest order oscillatory mode with symmetry of revolution and an antinode in the center of the flask. The vessel was modeled with flat end caps and no ports on them, so the cylinder length was approximated by an equivalent length (L_{eq}) obtained matching the volumes of the actual resonator and the simulated one. An example of the simulated acoustic field is shown in Fig. 5 for a cut in the *rz* plane and the radial intensity lobe in $z = L_{eq}/2$.

The next step in the numerical procedure was to identify the particular region of the $R_0 - P_{Ac}^{LF}|_b$ phase space defined by the conditions of our specific measurements. As mentioned earlier in the text, the relative concentration c_∞/c_0, $P_{Ac}^{HF}|_b$ and the relative phase ϕ were obtained from the numerical fit of experimental data traces of the bubble radius temporal evolution. An example of this is given in Fig. 6(a) for a single bubble spatially fixed using the eleventh harmonic ($N = 11$) which was slightly away from the pressure antinode. Then, the radius temporal evolution associated with the coordinates $\left(R_0; P_{Ac}^{LF}|_b\right)$ over the corresponding curve with the fitted value of c_∞/c_0, where bubbles are diffusively and shape stable, was simulated in order to compute the force field affecting those specific bubbles. In Fig. 6(b), the latter is represented with a highlighted curve, the hollow circle and square markers indicate the diffusive and the shape stability boundaries respectively, while

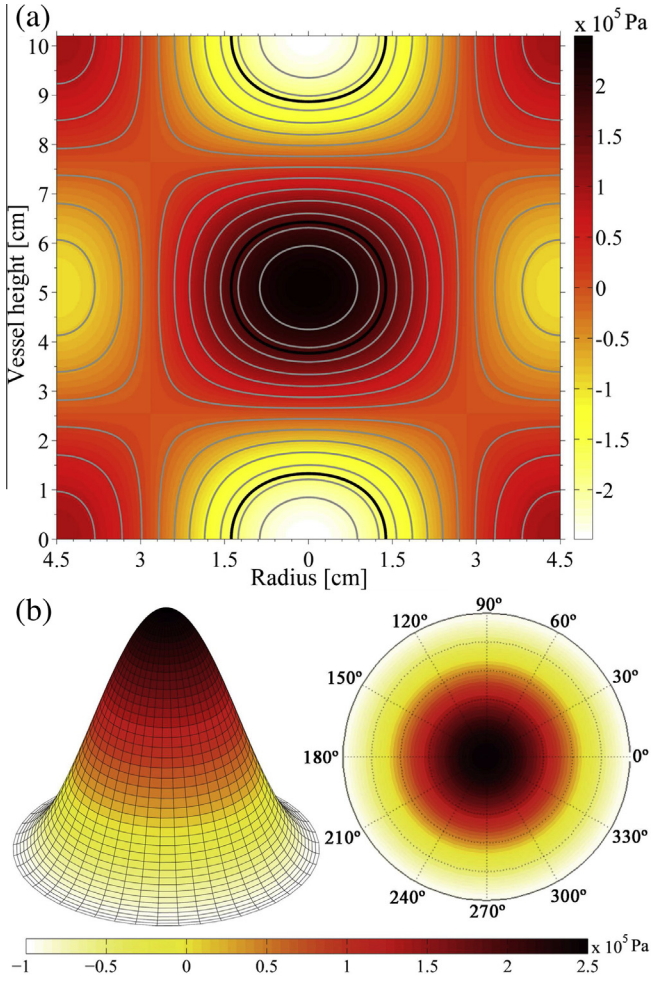

Fig. 5. Acoustic pressure amplitude in a cylindrical resonator computed using the solution of the linear wave equation, for the lowest oscillation mode with a pressure antinode in the geometrical center of the flask. The pressure amplitude at the main antinode was set in $P^{LF}_{Ac}|_0 = 2.5$ bar. (a) Acoustic pressure distribution in the plane rz. The gray solid lines are isobars. The black line represents the line with 1.74 bar which correspond to the acoustic pressure of the Bjerknes frontier ($\vec{F}_{Bj} = 0$) for the experimental data shown in Fig. 6. (b) Acoustic pressure for the horizontal plane ($r\theta$) at a middle height ($z = L_{eq}/2$).

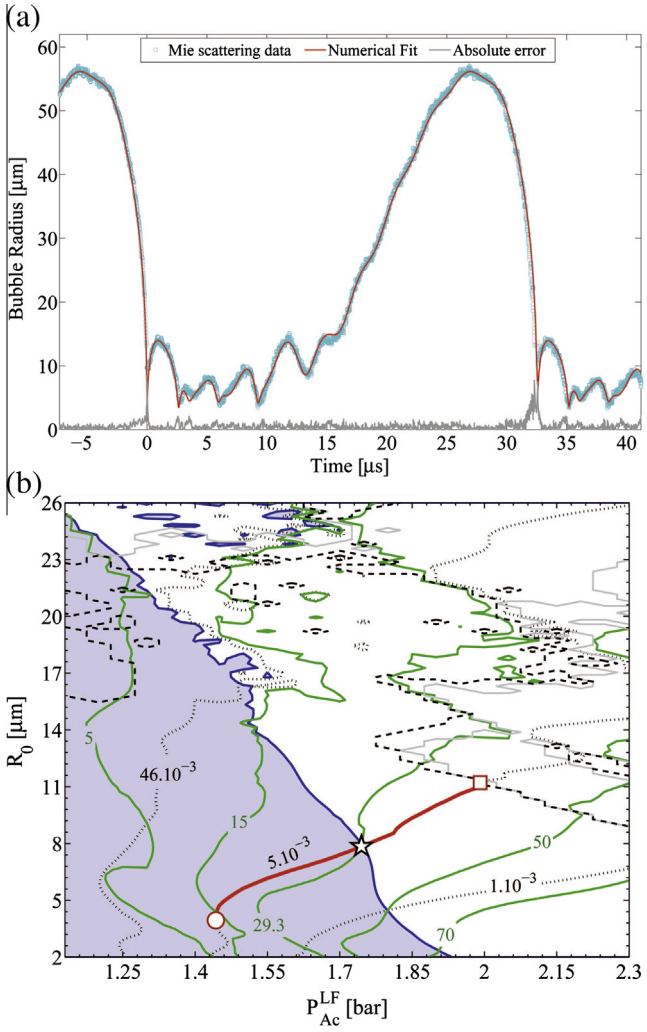

Fig. 6. Bubble dynamics for argon bubbles in SA85 for the case shown in Fig. 2. (a) Bubble radius temporal evolution obtained from Mie scattering. The bubble was driven using a biharmonic signal with $f_0 = 30{,}724$ Hz and the eleventh harmonic ($N = 11$). The experimental data is the average of 15 traces. The relative gas concentration obtained from the numerical fit was $c_\infty/c_0 \sim 5 \times 10^{-3}$ for $P_0 = 925$ mbar. The bubble was spatially fixed ~6 mm away from the antinode. The fitted parameters were: $R_0 = 7.8$ μm, $P^{LF}_{Ac}|_b = 1.74$ bar, $P^{HF}_{Ac}|_b = z1.65$ bar, $\phi = 0.25$ μs and $T_{max} = 29.3$ kK. (b) Computed $R_0 - P^{LF}_{Ac}|_b$ parameter map for the experimental parameters found in (a). The thin solid blue (black) line is the Bjerknes stability threshold ($\vec{F}_{Bj} = 0$). This line delimits the positionally stable region of the map (shaded in light blue (gray)) and the unstable region (uncolored). The solid line in light gray is the Rayleigh–Taylor shape instability for the mode $n = 2$. The dashed black line corresponds to the parametric shape instability threshold. In the latter two curves, the stable region is always below the lines, or outside the closed curves. The green (gray) solid curves are the contours of constant T_{max} (in units of kK) and the thin dotted curves (black) are the contours of constant c_∞/c_0. The thick solid red (dark gray) line joining the circle and square markers indicates all the possible coordinate pairs in the $R_0 - P^{LF}_{Ac}|_b$ phase space where the bubbles are diffusively and shape stable for $c_\infty/c_0 = 5 \times 10^{-3}$. The star marker indicates the experimental point shown in (a). (For interpretation of the references to color in this figure legend, the reader is referred to the web version of this article.)

the star marker locates the experimental point shown in Fig. 6(a). As it can be seen in Fig. 6(b), the experimental point lies just over the positional stability ($\vec{F}_{Bj} = 0$) frontier showing an excellent agreement between the observation and the calculation.

The complexities introduced by the non standard shape of our acoustic chamber, prevented us from accurately discriminating the oscillation mode associated with the HF component among the several matching possibilities when comparing the experimental frequency value against the theoretically approximated one [26]. As a consequence, the primary Bjerknes force was computed taking into account only the pressure gradient of P^{LF}_{Ac} (see Fig. 5). Besides, the HF component of the acoustic field (P^{HF}_{Ac}) was included through the radial bubble dynamics. Using the same approach to compute the Bjerknes force in the case of spherical symmetry, Dellavale et al. showed that the agreement between the observed bubble dynamics (e.g. the compression ratio R_{max}/R_0 and the time of collapse t_c) and the computed positional stability threshold improves for higher order harmonics (see Fig. 5 in [17] for $N > 5$). Moreover, as the order of the driving harmonic was increased, the aforementioned bubble parameters converge to those observed under single frequency driving ($f_0 \sim 30$ kHz). Accordingly, we did not observe a significant influence of the HF on the dimension of the clusters when higher order harmonics ($N \geqslant 9$) were used in the simulations.

Finally, the force field (Bjerknes, buoyancy) affecting the selected group of bubbles (highlighted curve in Fig. 6(b)) was simulated for the plane rz using the gradients of the computed acoustic pressure field for the main pressure antinode. In these simulations shown in Fig. 7, the positional stable region in which the Bjerknes force changes its behavior from repulsive to attractive, is defined as the outer perimeter of an axisymmetric oblate

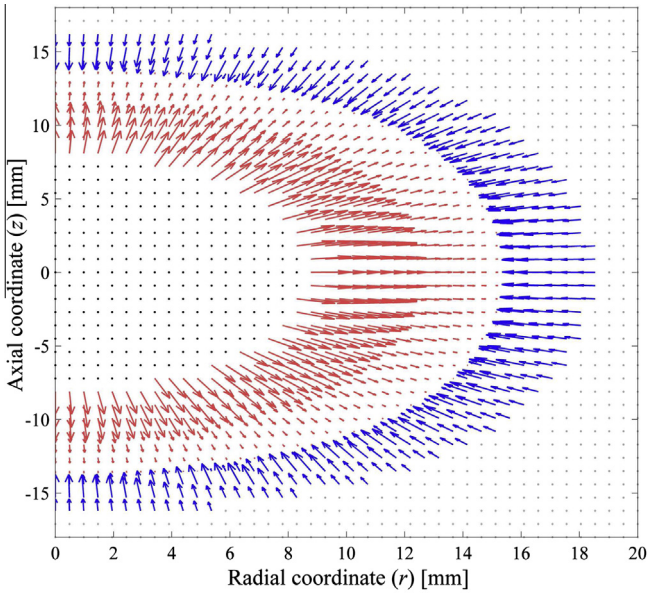

Fig. 7. Numerical simulation of the Bjerknes force field acting on bubbles with a relative gas concentration $c_\infty/c_0 \sim 5\times10^{-3}$ (red (dark gray) thick curve in Fig. 6(b)) for the case presented in Fig. 2 with f_0 = 30.73 kHz, N = 11 and $P_0 = 925$ mbar. The acoustic pressure field was calculated for the resonance mode shown in Fig. 5 and a pressure amplitude of $P_{Ac}^{LF}|_0 = 2.5$ bar. The lengths were measured with respect to the antinode. The black and gray dots correspond to regions of the $R_0 - P_{Ac}^{LF}|_b$ parameter space where bubbles cannot remain stable due to shape or diffusive instabilities respectively (e.g. ambient radius below the hollow circle marker and above the square marker in Fig. 6(b)). The light red (gray) and blue (black) vectors represent a repulsive and an attractive Bjerknes force (with respect to the antinode) respectively. The positionally stable zone, where the Bjerknes force is null, is given by an oblate ellipsoid. In the graph, this surface is defined by the points where the force vectors in a particular direction change their sense (and color) and the force switch from repulsive to attractive. (For interpretation of the references to color in this figure legend, the reader is referred to the web version of this article.)

ellipsoidal cluster centered closely to the acoustic field antinode, in agreement with the experimental observations (see Figs. 1–3). In the graph, this surface is defined by the points where the force vectors in a particular direction change their sense (and color). The light red (gray) and blue (black) vectors represent a repulsive and an attractive Bjerknes force (with respect to the pressure antinode) respectively. The black dots located close to the center of the ellipse represent the coordinate pairs $\left(R_0; P_{Ac}^{LF}|_b\right)$ with a constant gas concentration $c_\infty/c_0 \sim 5\times10^{-3}$ and pressures beyond the square marker in Fig. 6(b). In these regions, a bubble would be destroyed by the shape instability and can not exist in a stable fashion. Similarly, the gray dots are points of the phase space where the acoustic pressure is not high enough to sustain a diffusive equilibrium and a bubble under these conditions would eventually dissolve (region below the circle marker in Fig. 6(b)).

The role of possible bubble interactions were evaluated through the Secondary Bjerknes force ($\vec{F}_{Bj}^{(2)}$) following Refs. [6,31]. The Secondary Bjerknes force between two bubbles can be written as $\vec{F}_{Bj}^{(2)} = -\rho/4\pi\tau d^2 \int_\tau (\dot{V}_1(t))(\dot{V}_2(t))dt$, where ρ is the liquid mass density, d is the distance between bubbles, $\dot{V}_1(t)$ and $\dot{V}_2(t)$, represent the temporal derivative of the volume of the bubbles ($\dot{V}(t) = 4\pi R(t)^3/3$). Thus, the interaction force depends exclusively on the bubble dynamics (through $R(t)$ and the bubble wall velocity $\dot{R}(t)$) and not on the shape of the acoustic pressure field. As discussed in Refs. [6,31] $\vec{F}_{Bj}^{(2)}$ aims in the direction of the vector joining the bubble positions and is always attractive for equal size bubbles separated more than a distance of the order of 100 μm for SA (i.e. its magnitude is negative when $R_{01} = R_{02}$ and $d > 100$ μm). For the case of two bubbles over the oblate ellipsoidal cluster, the force vector $\vec{F}_{Bj}^{(2)}$ will have a component in the direction of the primary Bjerknes force (towards the center of the ellipsoid) regardless the bubble positions. Thus, in a cluster with uniformly distributed equal bubbles, this interaction force would act in the same way that the surface tension force, contracting the cluster. In order to determine how $\vec{F}_{Bj}^{(2)}$ affects the cluster size, we compute the interaction force on a bubble over the surface considering the contributions to the net force of first and second neighbors (because of the presence of the factor $1/d^2$ in the interaction force formula, higher order terms can be neglected without changing the result). We used a simulated $R(t)$ according to the experimental parameters for each case. In the latter, we did not include the interaction term in the Rayleigh–Plesset equation. This situation corresponds to an uncoupled case where the expansion suppressing effect is not significant and the $R(t)$ is barely modified [6]. Thus, taking into account that the collapse velocity and the maximum radius are decreased by the suppressing effect, the magnitudes of $\vec{F}_{Bj}^{(2)}$ computed with this approximation are overestimated, then represent an upper bound. According to the results in Ref. [31] this approximation is appropriate for high viscous fluids like SA85. In all the cases presented in this manuscript, the magnitude of the component of $\vec{F}_{Bj}^{(2)}$ in the direction of $\vec{F}_{Bj}$ was negligible comparing both forces. The distance which a bubble would need to move towards the antinode until $\vec{F}_{Bj}$ compensate the attraction force would be lesser than 0.1 mm in all cases (which is also lesser than the experimental error in the cluster size).

The numerical procedure described in this section allowed us to compare the cluster planar dimensions, i.e. the ellipse semi-axes, between the theoretically calculated and experimentally observed values for varying $P_{Ac}^{LF}|_0$ (Section 3.2.1), P_0 (Section 3.2.2) and c_∞/c_0 (Section 3.2.3). The length of the semi-axes in the ellipse-like experimental clusters was obtained fitting an ellipse over the photograph composed images. The measured lengths were corrected with the Snell law taking into account the distortion due to the vessel curvature and the refraction index of the liquid.

3.2.1. Simulations for different acoustic pressures

The dependence of the cluster dimensions on the acoustic pressure amplitude ($P_{Ac}^{LF}|_0$) was numerically studied for two experimental cases where the low-frequency voltage V_{PZT}^{LF} was varied, keeping V_{PZT}^{HF} unchanged ($\sim 84V_{rms}$). In the first case, the bi-frequency driving signal was constituted by f_0 = 30,724 Hz besides the eleventh harmonic (N = 11, $Q \simeq 2200$). In the second case, a fundamental frequency of f_0 = 30,628 Hz and the tenth harmonic (N = 10, $Q \simeq 1200$) were used to drive the bubbles. The acoustic pressures ($P_{Ac}^{LF}|_0$ and $P_{Ac}^{HF}|_0$) for the lowest value of V_{PZT}^{LF} used in each experimental trial ($V_{PZT}^{LF} \sim 23V_{rms}$), were obtained from a numerical fit of the Mie scattering data with the computed bubble radius temporal evolution (Fig. 6(a)). The fitted $P_{Ac}^{HF}|_0$ values were maintained constant during each set of numerical simulations being approximately 1.6 bar for N = 11 and 1.3 bar for N = 10. Then, taking into account that the characterized bubble was in a position of the standing acoustic field where it has positional equilibrium (elliptic black curve in Fig. 5(a)), we defined the acoustic pressure in that position ($P_{Ac}^{LF}|_{F_{Bj}=0} = P_{Ac}^{LF}|_b$ for $V_{PZT}^{LF} \sim 23V_{rms}$) as the limiting pressure associated to the frontier $\vec{F}_{Bj} = 0$ (see the star marker in Fig. 6(b)). Knowing $P_{Ac}^{LF}|_{F_{Bj}=0}$ and the distance from the position of the measured bubble to the center of the antinode from a photograph, we extrapolated the value of the acoustic pressure at the antinode $P_{Ac}^{LF}|_0^{EXT}$ by using the analytic expression of the acoustic field (i.e. $P_{Ac}^{LF}|_0$ for $V_{PZT}^{LF} \sim 23V_{rms}$). After that, we assumed that the acoustic pressure exerted over the bubbles composing the oblate surface would be the same limiting value $P_{Ac}^{LF}|_{F_{Bj}=0}$ for different PZT voltages [12] and then, we employed the analytical expression of P_{Ac}^{LF} within a cylindrical vessel to extrapolate $P_{Ac}^{LF}|_0$ for each V_{PZT}^{LF} using the vertical length of the experimental ellipses. We chose the vertical

length because it was better defined in the photographs. These extrapolated values $P^{LF}_{Ac}|^{EXT}_0$ lead to different simulated bubble cluster sizes which are compared to the experimental ellipsoidal surfaces in Fig. 8. The accordance between the experiments and the simulations was excellent, demonstrating that the bubbles lie very close to a null Bjerknes force surface. The variation of the cluster dimensions as a function of V^{LF}_{PZT} is clearly not linear. The relation of the extrapolated values of $P^{LF}_{Ac}|_0$ and V^{LF}_{PZT} was not linear either, having a similar behavior as the curves shown in Fig. 8. We also analyzed the ratio of the major semi-axis to the minor semi-axis (S) and found that the ellipsoidal surfaces expands (or shrinks) isotropically when $P^{LF}_{Ac}|_0$ is varied. For the case with $N = 10$ and $c_\infty/c_0 = 35 \times 10^{-3}$ the average ratio of the experimental clusters was $S^{exp}_{N=10} = (1.11 \pm 0.07)$ while the simulated ratio was $S^{num}_{N=10} = (1.095 \pm 0.002)$. For the case with $N = 11$ and $c_\infty/c_0 = 5 \times 10^{-3}$ the parameters S resulted $S^{exp}_{N=11} = (1.14 \pm 0.09)$ and $S^{num}_{N=11} = (1.103 \pm 0.003)$.

3.2.2. Simulations for different static pressures P_0

In this section, we studied the influence of the static pressure P_0 over the multi-bubble system. The numerical strategy was based on the overpressure method reported by Strasberg [3] and Greenspan et al. [4], and recently used by Herbert et al. [2] for the determination of the cavitation pressure threshold P_{cav}. In this method, the independence of P_{cav} from the static pressure P_0 is taken into account to establish a linear relationship between an equilibrium acoustic pressure amplitude $P^{LF}_{Ac}|^*_0$ and P_0, i.e. $P^{LF}_{Ac}|^*_0 = P_{cav} + P_0$. As detailed in Section 3.1.2, we performed measurements of bubble clusters for various values of P_0 imposing a fixed driving voltage of $V^{LF^*}_{PZT} = (60.0 \pm 0.4) V_{rms}$ to both generate and trap the bubbles. In these measurements, the continuous appearance of new cavitation bubbles lowered the effective acoustic pressure to a limiting value given by $P^{LF}_{Ac}|^*_0$. Thus, the number of SL bubbles and the acoustic pressure in the vessel was self regulated by the bubbles. Consequently, in order to simulate the force field acting over bubbles under different values of P_0, we had to set values for the parameters involved in the calculations: $P^{LF}_{Ac}|^*_0$, $P^{HF}_{Ac}|_0$, N, P_{cav} and c_∞/c_0. First of all, we obtained a relative gas concentration of $c_\infty/c_0 = 46 \times 10^{-3}$ and a value of $P^{HF}_{Ac}|_0 = 1.6$ bar from an experimental $R(t)$ fit for 925 mbar of P_0 and $N = 11$. Then, equivalent c_∞/c_0 values were computed for other static pressures employing Henrys Law. The cavitation pressure P_{cav} in our system was empirically determined by matching the dimensions of the simulated cluster to the experimental oblate ellipsoid corresponding to the case with $P_0 = 1500$ mbar (Fig. 3(d)). Since P_{cav} is independent of P_0, we were able to calculate the different values of $P^{LF}_{Ac}|^*_0$ for the other ellipsoids measured with others P_0 using the relation $P^{LF}_{Ac}|^*_0 = P_{cav} + P_0$. Fig. 9 presents the comparison of the dimensions of the simulated ellipsoids and the experimental ones. Using the discussed numerical strategy, a close agreement between simulation results and observed data was found. The average ratio S for the experimental clusters was $S^{exp}_{N=11} = (1.14 \pm 0.07)$ while the simulated ratio was $S^{num}_{N=11} = (1.11 \pm 0.01)$. Then, the isotropic behavior of the cluster size variation was also present in this case.

3.2.3. Simulations for different dissolved gas concentration in the fluid

Accurately setting a predefined value of dissolved gas concentration in the liquid has been proved to be very challenging in our experimental setup. This issue encouraged us to evaluate the dependence of c_∞/c_0 in the liquid on the bubble cluster size through numerical simulations. The coordinate pairs $\left(R_0; P^{LF}_{Ac}|_b\right)$ over different constant c_∞/c_0 curves in the $R_0 - P^{LF}_{Ac}|_b$ map were computed as previously explained in Section 3.2.

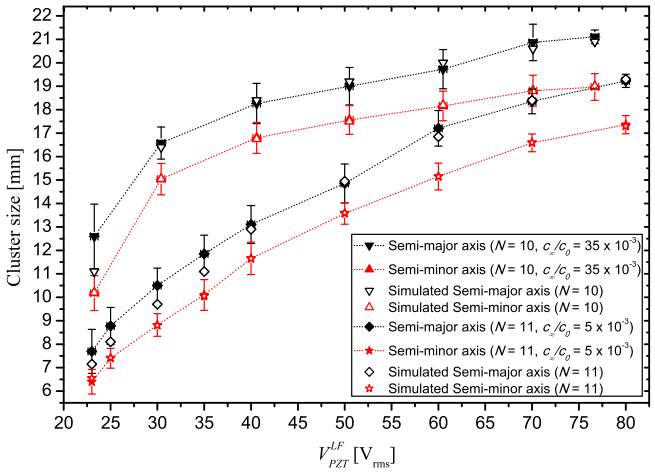

Fig. 8. Ellipsoidal bubble clusters dimensions for different acoustic pressures. The static pressure was 925 mbar. The longitude of the semi-axes of the experimental bubble clusters were obtained fitting an ellipse over the superimposed photographs. The measured lengths were corrected taking into account the distortion due to the resonator curvature and the refraction index of the liquid. The low-frequency component of the biharmonic excitation has $f_0 = 30{,}724$ Hz for the case with the eleventh harmonic ($N = 11$, $Q \simeq 2200$) and $f_0 = 30{,}628$ Hz for the case with the tenth harmonic ($N = 10$, $Q \simeq 1200$). The filled markers in the plot represent experimental values. The hollow markers indicate the results of the simulations, while the dotted line was drawn to ease the visualization of the data behavior. In the calculus, the acoustic pressures ($P^{LF}_{Ac}|_b$ and $P^{HF}_{Ac}|_b$) for the lowest value of V^{LF}_{PZT} used ($\sim 23 V_{rms}$), were obtained from a numerical fit of the Mie scattering data with the computed bubble radius temporal evolution (Fig. 6(a)). The $P^{HF}_{Ac}|_b$ values result approximately 1.6 bar for $N = 11$ and 1.3 bar for $N = 10$. For higher driving voltages $P^{LF}_{Ac}|_0$ were obtained by extrapolation with the analytical solution of the acoustic field and the experimental cluster dimensions.

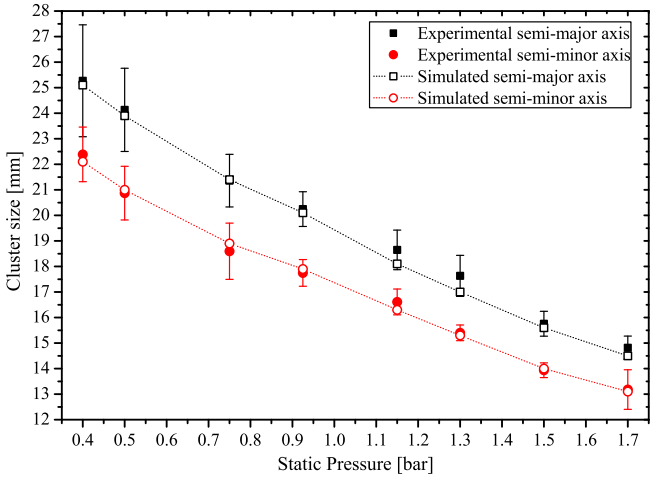

Fig. 9. Ellipsoidal bubble clusters dimensions for different static pressures. The longitude of the semi-axes of the bubble clusters were obtained fitting an ellipse over the superimposed photographs (e.g. Fig. 4). The filled black squares and red circles corresponds to the case where the applied low-frequency voltage remained fixed ($V^{LF^*}_{PZT} = (60.0 \pm 0.4) V_{rms}$) and the static pressure was varied between 0.4 bar and 1.7 bar. The hollow markers indicate the results of the simulations, while the dotted line was drawn to ease the visualization of the data behavior. The bi-frequency signal has $f_0 = 30.78$ kHz and the eleventh harmonic ($N = 11$). The experimental data indicates that the clusters dimensions are strongly affected for the static pressure. Furthermore, analyzing the ratio of the major and minor semi-axis (S) we realized that the cluster expands (or shrinks) isotropically when P_0 is varied. The parameter S for the experimental clusters was $S^{exp}_{N=11} = (1.14 \pm 0.07)$ while the ratio for the simulated null Bjerknes surfaces was $S^{num}_{N=11} = (1.11 \pm 0.01)$. In these measurements, an empirical acoustic cavitation pressure (P_{cav}) was determined by fitting an ellipse over the cluster with $P_0 = 1.5$ bar (Fig. 4(c)). Then, the different values of $P^{LF}_{Ac}|^*_0$ for distinct P_0 were calculated using the expression $P^{LF}_{Ac}|^*_0 = P_{cav} + P_0$. In addition, the concentration $c_\infty/c_0 = 46 \times 10^{-3}$ obtained from an experimental $R(t)$ fit for 925 mbar of P_0, was corrected for the other static pressures employing Henrys Law.

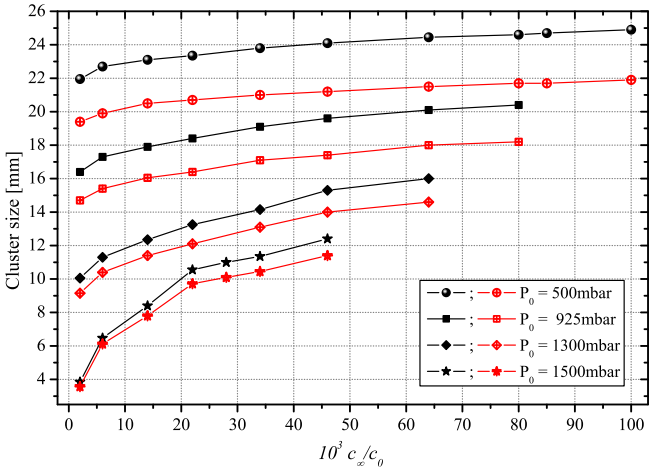

Fig. 10. Calculated cluster dimensions vs. c_∞/c_0 for different static pressures at a fixed acoustic amplitude $P_{Ac}^{LF}|_0 = 2.76$ bar, with $f_0 = 30.78$ kHz and $N = 11$. The filled symbols represent the length of the major axis in units of mm, while the minor axis length was indicated with open symbols. The dotted line was drawn to ease the visualization of the data behavior. For each curve shown, the upper limit of c_∞/c_0 corresponds to the relative concentration value in which the bubbles reach the shape instability before they become positionally unstable (i.e. the bubbles break up before get expelled from the pressure antinode).

The results of the simulations for the bubble cluster size with the following fixed parameters: $P_{Ac}^{LF}|_0 = 2.76$ bar, $P_{Ac}^{HF}|_0 = 1.4$ bar, $f_0 = 30.78$ kHz and $N = 11$ are shown in Fig. 10. For each curve shown in Fig. 10, the upper limit of c_∞/c_0 corresponds to the relative concentration value in which the bubbles reach the shape instability before they become positionally unstable (i.e. the bubbles break up before getting expelled from the pressure antinode). These simulations show that the change in the cluster dimensions varying c_∞/c_0 increases with a raise in P_0. However, that change becomes significant only for the lower concentrations analyzed, e.g. the variation of the cluster dimensions augmenting c_∞/c_0 in 50% (in the second half of the range) is lower than: 3% for 500 mbar, 5% for 925 mbar, 12% for 1300 mbar, 15% for 1500 mbar of P_0.

4. Conclusions

In this work, clusters of positionally and spatially stable sonoluminescent argon bubbles in a sulfuric acid aqueous solution (SA85w/w) were experimentally and theoretically studied. The degree of control over the multi-bubble system achieved in our experiment has no precedent in the current scientific literature. The controllability over the bubble clusters was exploited in order to study the positional and spatial bubble instabilities. We were able to generate these SL bubble clusters by applying a bi-frequency driving composed by the fundamental resonant frequency of the system f_0 and a high amplitude harmonic frequency component (Nf_0).

In order to give a theoretical framework to the size and shape of the bubble clusters for different acoustic pressures and various static pressures, a series of numerical simulations of the hydrodynamic forces acting on the bubbles were performed. The results of the simulations were in clear agreement with the experimental observations for both cases studied. The latter analysis allowed us to identify the primary Bjerknes force as the main force affecting the bubble cluster size. Furthermore, an experimental visualization of the null Bjerknes force surface predicted by numerical models for SA was achieved for the first time.

We performed trials with different harmonic frequencies (Nf_0) in the biharmonic driving signal. Particularly, we analyzed cases with the tenth or the eleventh harmonic of f_0 ($N = 10$ and $N = 11$, respectively). The main observations in the experiments of MBSL can be summarized as follows: (a) The low-frequency component of the acoustic pressure field has a significant influence over the positional stability of the bubbles constituting the clusters. (b) The effect of the driving high-frequency component over the positional stability was negligible for high order harmonics ($N \geqslant 9$). (c) We found that higher harmonics promoted a major number of SL cavitation bubbles forming the structure. (d) The HF component of the imposed acoustic pressure field enabled the removal of the spatial instability (pseudo-orbits) of the SL bubble cluster.

In the case where the applied acoustic pressure $P_{Ac}^{LF}|_0$ was increased, the cluster expands in order to preserve the conditions were the net force acting on the bubbles is zero (i.e. $P_{Ac}^{LF}|_b$ and R_0 remained constant). Regarding to the effect of static pressure over the bubble cluster, we found a significant reduction of the ellipsoidal cluster as P_0 was increased. This is explained by analyzing the changes occurring in the $R_0 - P_{Ac}^{LF}|_b$ parameter space for high static pressures. For elevated P_0 the positional stability frontier shifts to regions where higher acoustic pressures can be applied over the bubbles. As a consequence, the sonoluminescent bubbles can reach positions closer to the pressure antinode in the cylindrical flask. As we have shown in Ref. [19] this exposure of the bubbles to higher acoustic pressures enhances significantly the energy focusing in the bubble collapse. We also analyzed the ratio of the major to the minor semi-axis of the ellipsoids (S) and found that the ellipsoidal surfaces expands (or shrinks) isotropically when $P_{Ac}^{LF}|_0$ or P_0 were modified. Furthermore, we computed the magnitude of the component of $\vec{F}_{Bj}^{(2)}$ in the direction of $\vec{F}_{Bj}$, finding that the first one was negligible and did not change significantly the cluster dimensions. Finally, by means of extensive numerical simulations, we showed that the change in the cluster dimensions with varying c_∞/c_0 for different P_0 becomes significant only for lower concentrations and higher static pressure (relative to the analyzed range).

The experimental and numerical results presented in this paper are relevant in several current topics regarding to multi-bubble phenomena, e.g. forces acting over the bubbles in multi-frequency acoustic fields, the role of the relative phase between the driving signals, transient acoustic cavitation, bubble interactions, structure formation processes, atomic and molecular emissions of equal bubbles and nonlinear or unsteady acoustic pressure fields in bubbly media.

An important improvement over the present results should be achieved using a high Q rectangular acoustic chamber with multi-harmonic driving, since a regular periodic antinode structure would simplify the bubble distribution analysis and improve the degree of control over the bubble structure. The latter would be very useful to further understanding of bubble interaction phenomena. In addition, an acid resistant hydrophone would be useful to perform direct measurements of the acoustic pressure to complement the Mie scattering data.

Acknowledgements

We acknowledge Enrique Aburto who built the Pyrex vessels used in the experiments. We also thank Luciano Converti for his assistance in writing the image processing script. J.M.R. and D.D. were supported by CONICET.

References

[1] R.E. Apfel, The role of impurities in cavitation-threshold determination, J. Acoust. Soc. Am. 48 (5) (1970) 1179–1186.
[2] E. Herbert, S. Balibar, F. Caupin, Cavitation pressure in water, Phys. Rev. E 74 (2006) 041603.
[3] M. Strasberg, Onset of ultrasonic cavitation in tap water, J. Acoust. Soc. Am. 31 (2) (1959) 163–176.

[4] M. Greenspan, C.E. Tschiegg, Radiation-induced acoustic cavitation; apparatus and some results, J. Res. Natl. Bur. Stand. 71C (1967) 299–312; M. Greenspan, C.E. Tschiegg, Radiation-induced acoustic cavitation threshold versus temperature for some liquids, J. Acoust. Soc. Am. 72 (4) (1982) 1327–1331.
[5] J. Lee, M. Ashokkumar, K. Yasui, T. Tuziuti, T. Kozuka, A. Towata, Y. Iida, Development and optimization of acoustic bubble structures at high frequencies, Ultrason. Sonochem. 18 (2011) 92–98.
[6] R. Mettin, I. Akhatov, U. Parlitz, C. Ohl, W. Lauterborn, Bjerknes forces between small cavitation bubbles in a strong acoustic field, Phys. Rev. E 56 (3) (1997) 2924–2931.
[7] S.D. Hopkins, S.J. Putterman, B.A. Kappus, K.S. Suslick, C.G. Camara, Dynamics of a sonoluminescing bubble in sulfuric acid, Phys. Rev. Lett. 95 (2005) 254301.
[8] D.F. Gaitan, R.A. Tessien, R.A. Hiller, J. Gutierrez, C. Scott, H. Tardif, B. Callahan, T.J. Matula, L.A. Crum, R.G. Holt, C.C. Church, J.L. Raymond, Transient cavitation in high-quality-factor resonators at high static pressures, J. Acoust. Soc. Am. 127 (6) (2010) 3456–3465.
[9] V.F.J. Bjerknes, Fields of Force, Columbia University Press, New York, 1906.
[10] L.A. Crum, Bjerknes forces on bubbles in a stationary sound field, J. Acoust. Soc. Am. 57 (1975) 1363–1370.
[11] I. Akhatov, R. Mettin, C. Ohl, U. Parlitz, W. Lauterborn, Bjerknes force threshold for stable single bubble sonoluminescence, Phys. Rev. E 55 (1997) 3747–3750.
[12] R. Urteaga, D.H. Dellavale, G.F. Puente, F.J. Bonetto, Positional stability as the light emission limit in sonoluminescence with sulfuric acid, Phys. Rev. E 76 (2007) 056317.
[13] N.D. Flannigan, K. Suslick, Plasma formation and temperature measurement during single-bubble cavitation, Nature (London) 434 (2005) 52–55.
[14] A. Troia, D. Madonna Ripa, R. Spagnolo, Moving single bubble sonoluminescence in phosphoric acid and sulphuric acid solutions, Ultrason. Sonochem. 13 (2006) 278–282.
[15] R. Urteaga, F.J. Bonetto, Trapping an intensely bright, stable sonoluminescing bubble, Phys. Rev. Lett. 100 (2008) 074302.
[16] D. Dellavale, Algoritmos para el procesamiento concurrente de señales y su aplicación en sonoluminiscencia (Ph.D. Thesis), Instituto Balseiro, 2011.
[17] D. Dellavale, L. Rechiman, J.M. Rosselló, F. Bonetto, Upscaling energy concentration in multifrequency single-bubble sonoluminescence with strongly degassed sulfuric acid, Phys. Rev. E 86 (2012) 016320.
[18] L.M. Rechiman, D. Dellavale, F.J. Bonetto, Path suppression of strongly collapsing bubbles at finite and low Reynolds numbers, Phys. Rev. E 87 (2013) 063004.
[19] J.M. Rosselló, D. Dellavale, F.J. Bonetto, Energy concentration and positional stability of sonoluminescent bubbles in sulfuric acid for different static pressures, Phys. Rev. E 88 (2013) 033026.
[20] N.V. Dezhkunov, A. Francescutto, P. Ciuti, T.J. Mason, G. Iernetti, A.I. Kulak, Enhancement of sonoluminescence emission from a multibubble cavitation zone, Ultrason. Sonochem. 7 (2000) 19–24.
[21] P. Anderson, A. Sampathkumar, T.W. Murray, D.F. Gaitan, R.G. Holt, Optical nucleation of bubble clouds in a high pressure spherical resonator, J. Acoust. Soc. Am. 130 (5) (2011) 3389–3395.
[22] U. Parlitz, R. Mettin, S. Luther, I. Akhatov, M. Voss, W. Lauterborn, Spatio-temporal dynamics of acoustic cavitation bubble clouds, Philos. Trans. R. Soc. Lond. A 357 (1999) 313–334.
[23] W. Lauterborn, T. Kurz, Physics of bubble oscillations, Rep. Prog. Phys. 73 (2010) 106501.
[24] S. Hatanaka, K. Yasui, T. Kozuka, T. Tuziuti, H. Mitome, Influence of bubble clustering on multibubble sonoluminescence, Ultrasonics 40 (2002) 655660.
[25] K. Yasui, Y. Iida, T. Tuziuti, T. Kozuka, A. Towata, Strongly interacting bubbles under an ultrasonic horn, Phys. Rev. E 77 (2008) 016609.
[26] P. Birkin, T.G. Leighton, J.F. Power, M.D. Simpson, A.M.L. Vinotte, P.F. Joseph, Experimental and theoretical characterization of sonochemical cells. Part 1. Cylindrical reactors and their use to calculate the speed of sound in aqueous, J. Phys. Chem. A 107 (2003) 306–320.
[27] C.J.B. Vian, P.R. Birkin, T.G. Leighton, Cluster collapse in a cylindrical cell: correlating multibubble sonoluminescence, acoustic pressure, and erosion, J. Phys. Chem. C 114 (2010) 16416–16425.
[28] G.J. Posakony, L.R. Greenwood, S. Ahmed, Stable multibubble sonoluminescence bubble patterns, Ultrasonics 44 (2006) e445–e449.
[29] Y. An, Formulation of multibubble cavitation, Phys. Rev. E 83 (2011) 066313.
[30] M. Ida, Multibubble cavitation inception, Phys. Fluids 21 (2009) 113302.
[31] R. Sadighi-Bonabi, N. Rezaee, H. Ebrahimi, M. Mirheydari, Interaction of two oscillating sonoluminescence bubbles in sulfuric acid, Phys. Rev. E 82 (2010) 016316.
[32] W. Cheng-Hui, C. Jian-Chun, Interaction of a bubble and a bubble cluster in an ultrasonic field, Chin. Phys. B 22 (1) (2013) 014304.
[33] D. Rabaud, P. Thibault, M. Mathieu, P. Marmottant, Acoustically bound microuidic bubble crystals, Phys. Rev. Lett. 106 (2011) 134501.
[34] R.G. Holt, L.A. Crum, Mie scattering used to determine spherical bubble oscillations, Appl. Opt. 29 (1990) 4182.
[35] G.F. Puente, Sonoluminiscencia y cavitación en burbujas: Análisis dinámico y de estabilidad en regiones altamente no lineales (Ph.D. Thesis), Instituto Balseiro, 2005.
[36] G.F. Puente, R. Urteaga, F.J. Bonetto, Numerical and experimental study of dissociation in an air-water single-bubble sonoluminescence system, Phys. Rev. E 72 (2005) 046305.
[37] G.F. Puente, P. García-Martínez, F.J. Bonetto, Single-bubble sonoluminescence in sulfuric acid and water: bubble dynamics, stability, and continuous spectra, Phys. Rev. E 75 (2007) 016314.
[38] R. Mettin, A.A. Doinikov, Translational instability of a spherical bubble in a standing ultrasound wave, Appl Acoust 70 (2009) 1330–1339.
[39] M. Brenner, S. Hilgenfeldt, D. Lohse, Single-bubble sonoluminescence, Rev. Mod. Phys. 74 (2002) 425–484.